The Cryosphere Discuss., 6, 1871–1914, 2012
www.the-cryosphere-discuss.net/6/1871/2012/
doi:10.5194/tcd-6-1871-2012

The Cryosphere Discussions

A method for sea ice thickness and concentration analysis based on SAR data and a thermodynamic model

J. Karvonen[1], B. Cheng[1], T. Vihma[1], M. Arkett[2], and T. Carrieres[2]

[1]Finnish Meteorological Institute (FMI), Helsinki, PB 503, 00101, Finland
[2]Canadian Ice Service, 373 Sussex drive, Ottawa, Ontario K1A 0H3, Canada

Received: 2 April 2012 – Accepted: 8 May 2012 – Published: 31 May 2012

Correspondence to: J. Karvonen (juha.karvonen@fmi.fi)

Published by Copernicus Publications on behalf of the European Geosciences Union.

Abstract

An analysis of ice thickness distribution is a challenge, particularly in a seasonal sea ice zone with strongly dynamic ice motion field, such as the Gulf of St. Lawrence off Canada. We present a method for ice concentration and thickness analysis combining modelling of sea ice thermodynamics and detection of ice motion on the basis of space-borne Synthetic Aperture Radar (SAR) data. Thermodynamic evolution of sea ice thickness in the Gulf of St. Lawrence was simulated for two winters, 2002–2003 and 2008–2009. The basin-scale ice thickness was controlled by atmospheric forcing, but the spatial distribution of ice thickness and concentration could not be explained by thermodynamics only. SAR data were applied to detect ice motion and ice surface structure during these two winters. The SAR analysis is based on estimation of ice motion between SAR image pairs and analysis of the local SAR texture statistics. Including SAR data analysis brought a significant added value to the results based on thermodynamics only. Our novel method combining the thermodynamic modelling and SAR yielded results that well match with the distribution of observations based on airborne Electromagnetic Induction (EM) method. Compared to the present operational method of producing ice charts for the Gulf of St. Lawrence, which is based on visual interpretation of SAR data, the new method reveals much more detailed and physically based information on spatial distribution of ice thickness.

1 Introduction

Detailed information on sea ice conditions is crucial for navigation in ice-covered waters. The most important sea ice variables are the ice concentration, level ice thickness, and the amount and height of ridges. Hence, national operational ice services try to collect all available information on present ice conditions (ice analysis) and, with the help of prognostic dynamic-thermodynamic models, to forecast future ice conditions. The ice analysis is usually based on one or more of the following sources of information: coastal

TCD
6, 1871–1914, 2012

and ship-based in-situ observations on ice thickness, concentration, and ridges; satellite or airborne remote sensing data on ice thickness and concentration; and numerical model products. So far, however, the observational and model based information have been treated more or less in parallel, without many activities in interactive combination of the approaches. The ice analysis is typically illustrated via operational ice charts. The ice information illustrated in the ice charts differs between various national ice services, depending on the observations available and the practices developed. For example, the Finnish ice charts show the ice concentration, the average, maximum and minimum ice thickness, as well as the spatial distribution of different ice types. In addition, the level of ridging is characterized by a number from 1 to 5. In the Canadian Ice Service, the ice chart is in the form of the WMO egg code (Sandven and Jonannesen, 2006) presenting the concentration, stage of development, and predominant forms of up to 3–5 ice types for each selected geographical area. The Chinese ice charts for the Bohai Sea illustrate the isolines of ice thickness and ice edge as well as the ice drift velocity field (Luo et al., 2004).

In large sea areas with little navigation, remote sensing is the most powerful tool to collect information needed for an ice analysis, but challenges still remain. These depend on the type of remote sensing data available. In the case of passive microwave data, the detection of ice concentration is a challenge when it exceeds approximately 85 % (Andersen et al., 2007). The development of Synthetic Aperture Radar (SAR) methods have yielded a lot of advance, but problems still exist, among others, in the detection of ridges and measurement of ice thickness, above all the discrimination between thin and thick ice when both are deformed (Mäkynen and Hallikainen, 2004; Shokr, 2009).

The challenges in ice analysis also depend on the local conditions. The analysis is more difficult, if the ice thickness and concentration are strongly affected by both thermodynamics and dynamics. In seasonally ice-covered seas, the production of ice (basin-scale temporal evolution of ice thickness) is typically dominated by thermodynamic processes: the air-ice-ocean thermal interaction is crucial to determine the

TCD
6, 1871–1914, 2012

columnar and granular ice growth (Bitz et al., 2001). The spatial distributions of ice thickness and concentration are, however, often dominated by ice dynamics (Fischefet and Maqueda, 1997). A preliminary investigation of ice thickness analysis based on SAR data and a thermodynamic ice model has been made for the Baltic Sea (Karvonen et al., 2007, 2008).

In this study, a new method is presented for sea ice thickness and concentration analysis based on SAR data and a thermodynamic model. Here we address the seasonal sea ice cover in the Gulf of St. Lawrence (GSL) off Canada, but the methodology is applicable for all ice-covered seas with SAR data available. In the GSL the ice cover is more dynamic than in the Baltic Sea. Hence, the SAR-based method for the Baltic Sea (Karvonen et al., 2007, 2008) cannot be directly applied for the GSL, because ice motion detection from SAR data is also needed. First we present a new method to derive sea ice concentration and drift vectors on the basis of SAR data. In locations where the SAR data indicate presence of sea ice, a thermodynamic sea ice and snow model HIGHTSI is used to calculate the ice growth, forced by operational model products of the European Centre for Medium-Range Weather Forecasts (ECMWF). The thermodynamically based ice thickness is used as background information for the remote sensing algorithm. For the first time, we combine the SAR-based information and thermodynamic modelling of sea ice and its snow cover. The resulting sea ice thickness and concentration analysis are finally compared against airborne Electromagnetic Induction (EM) measurements and the present operational products of the Canadian Ice Service (CIS).

2 Study area, ice seasons, and data

The GSL is a seasonally ice-covered gulf at latitudes as low as 45.6–52.0° N (Fig. 1). Winter navigation in the GSL is active, as it is the pathway to St. Lawrence River providing access to Quebec City, Montreal, and the North American Great Lakes. Due to the high economic importance of navigation, there is a strong need to provide accurate

TCD
6, 1871–1914, 2012

sea ice analysis for the GSL. The dynamic sea ice cover in the GSL represents a challenging environment for an ice analysis.

Two winter seasons, 2002/2003 and 2008/2009 were selected for this study. The first one was a severe and the second one a mild winter. We had comprehensive data sets and supporting material covering both ice seasons from freeze-up to melt: SAR data, CIS ice charts, ice thickness measurements based on the EM device (Prinsenberg et al., 2002), and numerical weather prediction (NWP) products from the ECMWF. The SAR data consisted of 149 RADARSAT-1 images from 2002–2003, and 250 RADARSAT-2 images from 2008–2009. Both RADARSAT 1 and 2 operate at C-band (wavelength 38–75 mm); the wavelengths are 56 mm for RADARSAT-1 and 55 mm for RADARSAT-2 (slightly modified from that of RADARSAT-1 due to interference of RADARSAT-1 frequency with WLAN frequencies). The SAR images were ScanSAR images, which are made several hundreds of kilometres wide by combining several SAR beams. Because of the wide spatial coverage, these are most suitable for operational sea ice monitoring. The CIS ice charts were in a gridded format. The ice charts are primarily based on visual interpretation of satellite imagery and ice reconnaissance flights. The ice conditions are qualitatively illustrated by the standard WMO egg code over polygons defined by the CIS ice analysts in various parts of the GSL. A diagram of the WMO egg code is given in Fig. 2.

The quantitative mapping of the egg-code was made following the criteria given in Table 1, and the conversion of the egg-code total concentration (C_t) was made according to Table 2. The egg-code gives for each polygon the total concentration, partial concentrations, partial stages of development (related to the ice age), and partial predominant forms of ice. The segment total concentration value C_t was used as the concentration value in the comparisons, the ice thickness was derived from the stage of development, and for each segment the stage of development corresponding to the highest partial concentration was used in the mapping to ice thickness.

The quantified daily ice charts were interpolated to the HIGHTSI model domain (3111 grid cells, Fig. 1) and the ice thickness and concentration from each grid cell

TCD
6, 1871–1914, 2012

were extracted. Due to the dynamic sea ice cover in the GSL, the spatial distribution of ice thickness at a given time step is very complex and difficult to assess. The seasonal ice evolution, however, can be illustrated by the integrated basin-scale average ice thickness

$$Ha(t) = \frac{1}{N}\sum_{i=1}^{N} H_i(t), \quad (1)$$

where H_i is the ice thickness in the grid cell i, and N is the total grid number of grid cells (3111). Figure 3 shows the quantified CIS-based time series of ice extent as well as maximum and minimum ice thickness in the GSL for winter seasons 2002/2003 and 2008/2009.

Ice winter 2002/2003 was severe. The maximum values of ice extent and average basin scale ice thickness occurred in late March. In the early freezing season, the ice cover developed faster with respect to extent than thickness. During the melting season, however, ice thickness and extent decayed with the same rate. Ice winter 2008/2009 was mild; in early winter, ice extent increased faster than thickness. After the maximum ice cover was reached, the extent and thickness varied with the same rate until the final ice melt. The maximum ice extent and average ice thickness appeared in mid-March being in line with the ice climatology in the GSL.

3 Thermodynamic modelling

3.1 HIGHTSI model

A high-resolution thermodynamic snow and ice model (HIGHTSI) is used in this study to simulate thermodynamic ice growth and melt. HIGHTSI was initially developed to study snow and ice thermodynamics in seasonally ice-covered seas (Launiainen and Cheng, 1998; Vihma et al., 2002; Cheng et al., 2003, 2006). The model has been

TCD
6, 1871–1914, 2012

further developed to investigate snow and sea ice thermodynamics in the Arctic (Cheng et al., 2008a,b) and also lake ice (Yang et al., 2012; Semmler et al., 2012).

Ice and snow thickness, heat conductivity and temperature are simulated solving the heat conduction equations for multiple ice and snow layers. In addition, special attention is paid to the parametrization of the air-ice fluxes and the solar radiation penetrating into the snow and ice. The turbulent surface fluxes are parametrized taking the thermal stratification into account. The penetration of solar radiation into the snow and ice depends on the cloud cover, albedo, colour of ice (blue or white), and optical properties of snow and ice. The shortwave radiation penetrating through the surface layer is parametrized, making the model capable of quantitatively calculating sub-surface melting. Short- and long-wave radiative fluxes can either be parametrized or prescribed based on results of numerical weather prediction (NWP) models. The surface temperature is then solved from a detailed surface heat/mass balance equation, which is defined as the upper boundary condition and also used to determine whether surface melting occurs. At the lower boundary, the ice growth/melt is calculated on the basis of the difference between the ice-water heat flux and the conductive heat flux in the ice. In addition, snow-to-ice transformation through re-freezing of flooded or melted snow are considered in the model.

Model experiments in the Arctic Ocean have suggested that albedo schemes with sufficient complexity can more realistically reproduce basin-scale ice distributions (Liu et al., 2007). We applied a sophisticated albedo parametrization according to temperature, snow and ice thickness, solar zenith angle and atmospheric properties (Briegleb et al., 2004). The thermal conductivity of sea ice is parametrized according to (Pringle et al., 2007) and snow density and heat conductivity is calculated according to (Semmler et al., 2012).

In seasonally ice-covered seas, snow plays an important role in sea ice growth. On one hand, snow generates a strong insulation and prevents sea ice growth. On the other hand, snow may transform to granular ice due to refreezing of ocean flooding and

TCD
6, 1871–1914, 2012

snow melt, enhancing ice growth. A reliable calculation of snow depth heavily relies on precipitation, which is given as external forcing.

3.2 Forcing data and studied winter seasons

The atmospheric forcing for HIGHTSI was based on the operational analysis and short-term forecasts of the ECMWF. The analysis were available with 6 h intervals. The 2-m air temperature and humidity as well as the 10-m wind speed were applied to parametrize the turbulent fluxes of sensible and latent heat. The downward components of the solar shortwave and thermal long-wave radiation were based on 12-h operational forecasts. To avoid spin-up problems in precipitation (Tietäväinen and Vihma, 2008), snow fall was based on 24-h forecasts. We selected the ECMWF products as forcing for HIGHTSI, because previous studies have demonstrated that they are of comparatively high quality even at high latitudes (Bromwich et al., 2009; Cheng et al., 2008a; Jakobson et al., 2012). To get an idea of the accuracy of the ECMWF products in the GSL, the wind speed (V_a) and air temperature (T_a) at selected locations were compared with results of the Environment Canada regional operational forecast model (in 15 km resolution). The results of the ECMWF and Environment Canada models agreed very well. The correlation coefficient between ECMWF and CIS modelled basin-scale wind speed and air temperature were 0.97 and 0.98, respectively, for both the winter seasons. The basin-scale ECMWF average air temperature for the entire winter seasons 2002/2003 and 2008/2009 were −2.1 °C and −0.8 °C, while the corresponding values from CIS regional model were −2.9 °C and −1.2 °C, respectively. The average wind speed for the winter 2002/2003 from the ECMWF result was 8.4 $m s^{-1}$ versus 8.0 $m s^{-1}$ from the CIS regional model. For winter 2008/2009 the corresponding values were 8.6 $m s^{-1}$ (ECMWF) and 8.3 $m s^{-1}$ (CIS).

To carry out HIGHTSI experiments over the entire GSL, atmospheric forcing is needed over a high-resolution grid. The ECMWF analysis and forecasts were available with a horizontal resolution of 0.358° for winter 2002/2003 and 0.225° for winter 2008–2009, whereas HIGHTSI was applied in a resolution of 0.225° in longitude and

TCD
6, 1871–1914, 2012

0.1125° in latitude. Hence, the ECMWF forcing fields were linearly interpolated to the HIGHTSI grid.

3.3 Model experiments

HIGHTSI experiments were carried out at each of the 3111 grid cells. Each model run starts 1 December and lasts until 31 May. The experiments are initialized with a thin ice layer (0.01 m) at each grid cell. If the external weather data do not favour ice growth, HIGHTSI resumes the initial ice thickness. Off the coastal land-fast ice zone, ice drifts significantly in the GSL. The impact of ice drift is taken into account by incorporating sea ice concentration (A) derived from SAR data into the HIGHTSI model. When a grid cell is at least partly covered by ice ($A > 10\,\%$), the ice growth is calculated applying the atmospheric forcing at that particular grid cell. If the ice concentration at a certain grid cell is reduced below 10 %, the ice thickness will remain at the value of the previous time step. The calculation of ice growth is resumed once the ice concentration is again larger than 10 %. The oceanic heat flux is parametrized as a function of the SAR-based ice concentration. This assumption is related to the low latitudes of 46–52° N, where increasing amounts of open water are usually associated with increasing solar energy absorbed by the ocean, consequently increasing the oceanic heat flux.

Figure 4 shows the modelled basin-scale average ice thickness compared with the quantified mean ice thickness from CIS ice charts. For the cold winter season 2002/2003, the modelled ice thickness showed a reasonable agreement with CIS ice charts, except in March, when the ice thickness was underestimated by up to 50 %. For the mild winter 2008/2009, the HIGHTSI model run showed a better agreement with CIS ice charts. For a cold winter, the large ice growth may be associated with frequent high pressure conditions, which are associated with less precipitation. On the contrary, a mild winter is usually associated with low pressure conditions, which means frequent cases of advection of warm, moist marine air masses, bringing more precipitation (snowfall). The ECMWF accumulated snowfall in winter 2008/2009 was 334 mm water equivalent, which was 45 % more than in winter 2002/2003 (231 mm). The role of

TCD
6, 1871–1914, 2012

snow may generate uncertainties due to potential errors in the NWP-based modelled precipitation.

We emphasize that the HIGHTSI-based ice thickness only accounts for the thermodynamic growth and melt. The dynamic ice growth such as rafting and ridging are taken into account by ice motion detection using SAR data. The HIGHTSI model runs are used as background information for the remote sensing algorithm described in the following section.

4 SAR remote sensing

In the experiment we used HH-polarized (SAR antenna transmitting horizontally polarized and receiving horizontally polarized signal) SAR data from RADARSAT-1 (season 2002–2003) and RADARSAT-2 (2008–2009). RADARSAT-2 has an option to acquire dual-polarized images in the wide swath imaging mode, but we only had dual-polarized data (HH/HV polarization combination, HV denotes transmitting horizontally polarized and receiving vertically polarized signal) over a short period (a few weeks in late February and early March 2009) at our disposal, and in this experiment we only utilized HH-polarized data, including the HH-channel data of the 2009 HH/HV data. Three SAR algorithms were used in this experiment. The first SAR algorithm estimates the ice concentration, based on SAR texture features. This concentration is used as an input for the HIGHTSI model and also for the ice thickness estimation. The SAR ice drift algorithm estimates the ice drift between two co-registered SAR images acquired over the same area at different time instants. The ice thickness estimation method presented here is a novel method combining the remote sensing and model data. The SAR ice thickness algorithm estimates the ice thickness using the modeled ice thickness distribution, kinematic features based on the SAR ice drift, SAR features, and SAR ice concentration as input.

TCD
6, 1871–1914, 2012

4.1 SAR data preprocessing

The SAR images are first calibrated to get the logarithmic backscattering coefficient values, which are presented in decibels. The backscattering coefficient, σ^0, describes the properties of the target area producing the backscatter of each SAR pixel. The σ^0 values are then linearly scaled to eight bits per pixel (8 bpp) images, the scaling interval is from −35 dB to 0 dB. The general calibration equations are:

$$\sigma^0 = \frac{A^2}{K}\sin(\alpha) = \frac{I}{K}\sin(\alpha), \quad (2)$$

$$\sigma^0(\mathrm{dB}) = 10\log_{10}(\sigma^0). \quad (3)$$

K is a SAR calibration coefficient, and typically given in the SAR metadata, A is the SAR amplitude value and $I = A^2$ is the SAR intensity value. α is the SAR incidence angle, which increases from the near range to far range, and typically varies about in the range of 20–50°. The 8 bpp SAR images are then rectified to Lambert Conformal Conic (LCC) projection. After rectification, a land masking to mask off all the land areas is applied. The land masking was based on the GSHHS shoreline (Wessel and Smith, 1996).

After calibration, rectification and land masking, we also apply an incidence angle correction (Mäkynen et al., 2002), which is based on an empirical linear relationship between mean sea ice backscattering and incidence angle value. After incidence angle correction we build daily mosaics of the SAR data in a constant grid in 500 m resolution in the LCC projection. The mosaics are used as inputs for the ice concentration and ice thickness estimation. An example of a SAR mosaic is shown in Fig. 5.

The SAR mosaics are also segmented. Here we use a simple k-means clustering (MacQueen, 1967) for the segmentation with the parameter value $k = 10$. The small segments are then removed iteratively, starting from the smallest ones, joining them to the larger segments with the closest mean corrected backscatter value. The size (in pixels) for the segments to be joined is increased iteratively starting from one and

TCD
6, 1871–1914, 2012

ending to the given upper limit. We have used the upper limit of 100 pixels, i.e. the segments smaller than 100 pixels are joined to the neighboring segments. The segmentation is an important stage of the SAR processing, because the ice concentration and thickness are estimated for each SAR segment, instead of single pixels. We use a lower bound for the segment size because it is necessary to have large enough number of points to compute reliable statistics and computing over segments maintains the natural ice segment boundaries unlike computing over regular data windows of a fixed size.

4.2 Ice motion detection

The ice motion estimation algorithm is based on phase correlation computed in two resolutions. First the larger-scale ice motion is detected in the coarse resolution, and then it is refined in the fine resolution. A multi-resolution phase-correlation algorithm for sea ice drift estimation was also presented in (Thomas et al., 2004). In our approach, the phase correlation computation is performed for edged areas only, because these typically are the areas, where reasonable correlations can be computed. In smooth or random areas the correlations are too low for reliable drift detection.

The edges are here detected using the Canny edge detection algorithm (Canny, 1986), but in practice most of the edge detection algorithms produce similar results. Typically the edge detection is based on gradient magnitude in the images. After edge detection, we perform a filtering of the edges, filtering out small edge segments. An edge segment is here defined as a set of connected edge pixels, in the sense of the pixel's 8-neighborhood. All the edge segments smaller than a given size (an integer number of pixels) are removed from the edge image. A suitable size threshold for a full-resolution SAR edge image is five. The small edge segments are typically due to speckle and do not describe any actual SAR features.

The ice motion is then determined for sampled data windows from the two images using the phase correlation in both resolutions. The window size is $W \times W$ pixels; we use $W = 16$. To compute the phase correlation 2-D FFT is applied to the data windows

TCD
6, 1871–1914, 2012

sampled from the two co-registered images at the same location. Then FFT-coefficients of the two image windows are normalized by their magnitudes, and the FFT-coefficients of the two image windows are multiplied and the inverse 2-D FFT is applied, i.e. the phase correlation (PC) array is computed from the the normalized cross power spectrum. The best matching displacement in a Cartesian (x, y) coordinate system is defined by the maximum PC:

$$\begin{aligned}(\mathrm{d}x, \mathrm{d}y) &= \arg\max_{(x,y)} \{\mathrm{PC}(x,y)\} \\ &= \arg\max_{(x,y)} \left\{ \mathrm{FFT}^{-1} \left(\frac{(X_1^*(k,l) X_2(k,l))}{|X_1^*(k,l) X_2(k,l)|} \right) \right\}, \end{aligned} \quad (4)$$

To get the low resolution images, the two co-registered images are first down-sampled to the given resolution. The down-sampling ratio R_S is a power of two; we use $R_S = 16$. The two low resolution images are generated by successively applying a half-band low-pass FIR filter designed for multi-resolution image processing (Biazzi et al., 1998). Multiple PC maxima, defined by a threshold (lower bound) for the PC, for each low resolution level location are saved and delivered to the high-resolution level as candidates of the coarse motion. The number of PC candidates for a location with row and column coordinates (r, c) in the grid is denoted by $M_{(\mathrm{r,c})}$.

At the fine resolution level, all the motion candidates at each location from the low resolution level, scaled up by the down-sampling factor are considered as potential low resolution ice drift candidates, and the windows are sampled in a $W/2 \times W/2$ pixel grid from the full-scale first image (i.e. the step resolution is 800 m for images with 100 m resolution), and the sampling locations from the second image are defined by the M scaled displacements from the low resolution. The fine resolution ice motion is the motion corresponding to the maximum high-resolution PC taking into account all the $M_{(\mathrm{r,c})}$ motion candidates from the low resolution.

Finally, a vector median filtering (Astola et al., 1990) is performed in the high-resolution ice motion grid, with a given radius, to obtain the final motion estimate. The size of the filtering is dependent on a quality index, computed for each motion estimate, and is varied from 5×5 to 11×11 points in the fine resolution motion grid. The areas

TCD
6, 1871–1914, 2012

with lower quality value use larger vector median computation window. A more detailed description of the SAR ice motion algorithm and some validation results can be found in (Karvonen, 2012a).

Divergence (D) and shear (S) of ice motion are calculated approximating the spatial derivatives by finite differences in the grid. Then the total deformation can then be computed as

$$D_{\mathrm{T}}(F) = \sqrt{S^2 + D^2}. \quad (5)$$

Another feature derived from the ice drift is the ice drift ratio, denoted by R_M at each grid position (r, c):

$$R_M(\mathrm{r},\mathrm{c}) = \sum_{i=t_o}^{t_n} |\mathbf{f}_i(\mathrm{r},\mathrm{c})| / \left| \sum_{i=t_o}^{t_n} \mathbf{f}_i(\mathrm{r},\mathrm{c}) \right| - 1. \quad (6)$$

One is subtracted just to make change the lower bound of the values of R_H to zero instead of one (the numerator is always larger than or equal to the denominator).

4.3 SAR-based ice concentration

For the ice concentration detection we have used two SAR texture features. The first is the relative amount of edge and corner points with respect to the segment size for each SAR segment. The edges and corners are detected based on a variant of the Local Binary Patterns (LBP) texture measure (Ojala et al., 1996). In this version the LBP patterns are formed such that a threshold (T) for the absolute difference between the middle point and the reference points is applied; here we use $T = 10$. The reference points are the eight points with the angular step of $\Pi/4$ around the middle point within a given distance R; we use $R = 2$. After computing the local binary pattern for each pixel location, the minimum of all the cyclic shifts of the eight-bit number is selected as the LBP for the pixel, this operation makes the values rotationally invariant. These

TCD
6, 1871–1914, 2012

LBP values can then be interpreted as edges (LBP value 15), corners (31) and sharp corners (63). The relative number of edge points within a segment is then the number of the points with the above-mentioned values N_e divided by the area segment A, computed in pixels:

$$F_e = N_e/A. \quad (7)$$

The other texture feature is based on the three gradient features computed in fixed-size round-shaped (here radius $R = 5$) data windows over the SAR image at each image location. The features we use are the relative amount of high gradients (or edges) within a window (GF_1), the optimal threshold between the high and low gradient parts (GF_2), the high gradient area (or edge) shape (GF_3). It is assumed that each pixel contains an edge and some background pixels. The pixels with high absolute gradient values are the edge pixels and the pixels with the low gradient values are the background pixels. We also assume that there are pixels from one edge in each small window and that both the edge and background absolute gradient values have a Gaussian distribution. Based on the assumption we apply the Expectation-Maximization algorithm (Dempster et al., 1977) to find the parameters of the two Gaussian distributions for each window. The features are then derived based on the edge and background pixels at each SAR location. The gradient texture features are described in more detail in (Karvonen, 2012b). In the classification we use segment means of the gradient texture features.

The texture feature we have used in concentration estimation is the gradient feature magnitude M_g:

$$M_g = \sqrt{GF_1^2 + GF_2^2 + GF_3^2}. \quad (8)$$

As an input for the concentration estimation we use the maximum of the two texture features, i.e. $F = \max(F_a, M_g)$. The concentration C is estimated with an experimental

TCD
6, 1871–1914, 2012

relationship:

$$C = \begin{cases} 0, & \text{if } F < T_1, \\ a_c F, & \text{if } T_1 \le F \le T_2, \\ 100, & \text{if } F > T_2. \end{cases} \quad (9)$$

Here we have used $T_1 = 10$ and $T_2 = 30$. The factor a_c is defined such that C is continuous at T_1 and T_2.

Open water areas can then simply be found by thresholding the concentration. Here we use 50 % as the threshold.

On the basis of comparison with visual interpretation of CIS ice charts, the ice concentration estimation seems to work well. Some overestimation of the ice concentration may occur in the melting period. The reliability of the concentration can be improved if there are multiple SAR images over the same area with a relatively short temporal difference. Then e.g. the temporal medians of the features can be used instead of the features from single SAR measurement, making the estimation more robust, especially over open water areas with occasional short wavelength (wavelengths in the magnitude of the SAR wavelength) wave patterns.

5 SAR and model based ice thickness

The correlation between SAR backscattering and different ice types is not always very high (Mäkynen and Hallikainen, 2004; Shokr, 2009); for this reason it is necessary to utilize ice motion and SAR texture features in the ice thickness estimation. Our ice thickness algorithm utilizes the SAR features, ice thickness modeled by HIGHTSI, kinematic ice features derived from the SAR based ice drift, and ice concentration from the SAR ice concentration algorithm. A general flow chart of the ice thickness algorithm is presented in Fig. 6.

In the first phase, the HIGHTSI ice thickness is redistributed based on several image features, computed over the mosaics of a period of two weeks before the mosaic of

TCD
6, 1871–1914, 2012

each day. These statistics represent the cumulative ice dynamics during each two week period. The features computed from the ice motion are the drift ratio R_M over the period, total deformation D_T, mean SAR pixel value μ (with incidence angle correction) over the period, and mean relative amount of edges E over the period. The geometric mean of these features is then used to form a new feature F_1 for each pixel, whose row and color coordinates are (r, c):

$$F_1(r,c) = (R_H(r,c)D_T(r,c)\mu(r,c)E(r,c))^{1/4}. \quad (10)$$

The final feature F_1 is used in a relative manner. The cumulative distributions of the HIGHTSI ice thickness and the distribution of the feature are mapped to the ice thickness so that the Kolmogorov-Smirnov distance (DeGroot, 1991) between the HIGHTSI ice thickness distribution and the mapped feature distributions is minimized. This redistributed ice thickness is then used as an input for the daily ice thickness estimation.

In the final phase the coefficient of variation C_v, i.e. the ratio of the local (here the segment-wise) standard deviation and the local mean (in percents), is used as an additional texture feature:

$$C_v(r,c) = 100\ \sigma(r,c)/\mu(r,c), \quad (11)$$

where $\mu(r,c)$ and $\sigma(r,c)$ are the local mean and standard deviation, respectively, computed for the segment in which the pixel at (r, c) belongs. This feature is also quite robust against variations due to incidence angle. The incidence angle corrected SAR pixel value mosaic $P(r,c)$ is modulated by $C_v(r,c)$ (geometric mean) and this value $F_2(r,c)$ is used in the thickness estimation:

$$F_2(r,c) = (C_v(r,c)P(r,c))^{1/2}. \quad (12)$$

The redistributed HIGHTSI thickness values H_h are modified based on the value of F_2 to get the ice thickness estimate H at (r, c):

$$H(r,c) = a\ (H_h(r,c)F_2(r,c))^{1/2} + b. \quad (13)$$

TCD
6, 1871–1914, 2012

Here $a = 5.52$ and $b - 112.85$. These parameters were defined based on the 2003 EM data and the $(H_h F_2)^{1/2}$ distributions. The distributions were first estimated by smoothing the distributions with a Gaussian kernel with a standard deviation of 10.0. Then the means and standard deviations for the two distributions (denoted by μ_1, μ_2, σ_1, and σ_2) were computed. Assuming, for simplicity, that the distributions are Gaussian, we get the scaling factors between the distributions:

$$a = \sigma_2/\sigma_1, \tag{14}$$

$$b = \mu_2 - (\sigma_2/\sigma_1)\mu_1. \tag{15}$$

6 Comparisons against CIS ice charts and EM data

6.1 CIS ice charts

We had the CIS ice charts for the two test winters in a gridded format, and we made some qualitative comparisons against the ice thickness values derived from the ice chart information on the stage of ice development. We used the total concentration C_t, and the ice thickness values were extracted from the ice charts as described in Sect. 2.

We see from Figs. 7–10 that concentrations from the SAR algorithm correspond to the concentrations extracted from the CIS ice charts rather well. In the ice thickness, however, there are large differences in certain areas. One of the reasons for this is that the ice drift was estimated in a resolution of 8 km (corresponding to the motion estimation algorithm window size multiplied by the SAR mosaic resolution, i.e. 16 × 500 m) and the motion in narrow straits and river outflows can't be detected, and the HIGHTSI remapping in these areas fails. This could probably be improved by estimating the motion in a higher resolution (now we have used the 500 m mosaic resolution).

TCD
6, 1871–1914, 2012

6.2 EM measurements

The electromagnetic induction (EM) ice thickness measurements made over the GSL during the two seasons (Prinsenberg et al., 2002) were used as a reference data set. EM measurements are considered as one of the most accurate methods to measure sea ice thickness over a large area that cannot be covered by drilling (Pfaffling et al., 2006; Haas et al., 2006). In both winters, the EM measurements were made within a relatively short period of 1–2 weeks from late February to early March. The measurements were made close to the Prince Edward Island, and were mainly headed to the north of the island (Fig. 11). The sampling rate of the EM measurements was 3–4 m and the resolution (footprint) was around 20–30 m.

The ice thickness values were compared to EM thickness measurements made in the GSL in 2003 and 2009. Applying a sliding median window along the EM measurement line, the EM measurements were smoothed to a resolution similar to that of the SAR data mosaics (500 m). The combined comparisons along the EM measurement lines are shown in Fig. 12.

The EM data from 2009 are independent, but the 2003 data were used for defining the mapping coefficients from the SAR features and HIGHTSI results to the ice thickness estimates. In general, the SAR algorithm overestimates the ice thickness, for the test data of 2009 the mean overestimation was 16.7 cm, and for the 2003 data 6.6 cm. It also seems that there are some shifts between the EM measurements and SAR thickness estimates. This is probably due to the ice motion and temporal differences (the mosaics contain data from multiple SAR images with different acquisition times) between the EM measurement and the SAR acquisition. Registration inaccuracies between the EM and SAR data sets are also possible.

Because it seems that direct pixel-wise comparison does not give very convincing error statistics (due to the above-mentioned shifts), we also compared the ice thickness distributions based on the SAR algorithm, CIS ice charts, HIGHTSI experiments, and EM ice thickness measurements. The comparison was limited to the EM measurement

TCD
6, 1871–1914, 2012

lines. We computed the Kolmogorov-Smirnov statistics between the EM ice thickness distribution, the CIS ice chart mean ice thickness, and the HIGHTSI ice thickness. The Kolmogorov-Smirnov statistics D_n between two cumulative distribution functions $F_n(x)$ and $F(x)$ is

$$D_n = \sup_x |F_n(x) - F(x)|, \quad (16)$$

here the cumulative distributions are also functions of the ice thickness. The Kolmogorov-Smirnov statistics are tabulated in Table 3, the mean ice thickness along the EM flight lines are tabulated in Table 4, and the comparison of the ice thickness distributions is shown in Fig. 13.

Compared to the CIS ice charts and the solely thermodynamic results, the agreement between the EM data and the new method is excellent. The results of the new method for the test season 2008–2009 ice thickness distribution even have a slightly better Kolmogorov-Smirnov statistics than those for the the season 2002–2003, used in estimation of the algorithm parameters. The mean ice thickness for the season 2008–2009 is, however, overestimated more (see Table 4) than for the season 2002–2003.

7 Conclusions

We developed a novel methodology for deriving sea ice parameters based on a thermodynamic ice model and SAR data in a fully automated manner over GSL. Our algorithms compute estimates for the ice concentration and ice thickness utilizing input data from a thermodynamic ice model, SAR based ice motion, and SAR texture features. We applied the method for the GSL with promising results.

The HIGHTSI-based ice thickness is only affected by thermodynamics. Ice dynamics was considered by incorporating ice concentration information from SAR data analysis. In the basin scale, the modelled evolution of ice thickness was comparable with that based on the CIS ice charts. The results suggested that the seasonal evolution of ice thickness and extent are largely dominated by the weather forcing conditions. The main

TCD
6, 1871–1914, 2012

sources of uncertainty in the model experiments were the amount of snow fall and the oceanic heat flux.

The results of the SAR-based ice concentration estimation were promising. If there are multiple SAR images over the same area with a reasonable temporal gap available, the ice concentration estimates can be further improved by using a temporal minimum over a short time period. The reasonable temporal gap depends on the conditions; in the freezing and melting periods it could be about one day, and in the mid-season several days.

The ice thickness estimation also produced promising results: validation against the local EM measurements showed that the ice thickness based on the new method was much more realistic than that based on the CIS ice charts. A problem in SAR based ice thickness estimation is, however, to locate areas of thin ice. SAR backscattering and texture for deformed thin ice is sometimes very similar to the values for thick deformed ice areas. We have tried to address this problem by utilizing the ice drift from SAR data together with the thermodynamic ice model. However, the coarse resolution of the ice drift used here cannot yield proper ice drift information over narrow sea areas (straits) present in the GSL. Also the temporal resolution of SAR is varying from half a day to several days, and thus the SAR based ice drift can only yield reliable statistics over periods of a few weeks. Hence, rapid dynamic events can only be detected on the basis of SAR texture interpretation. It has been shown that radiometer data can be used for estimation of the thin ice thickness (Yu and Rothrock, 1996; Kaleschke et al., 2010; Mäkynen et al., 2010), and combining this information with the SAR would be useful in thin ice thickness estimation. The estimation of the ice thickness from radiometric data is based on the surface temperature, derived from the observed brightness temperatures, and heat flux calculations.

An alternative approach would be to make the ice analysis on the basis of observations and a dynamic-thermodynamic model. Modelling of ice dynamics in a complex coastal or archipelago region is, however, very challenging (Gao et al., 2011). Our method is, however, not affected by the error sources of modelling sea ice dynamics.

TCD
6, 1871–1914, 2012

We think that the SAR ice thickness estimation algorithm has potential for operational use. The main challenge towards operational sea ice thickness algorithms is probably the lack of in-situ measurements for proper algorithm calibration and validation. To build a reliable operational system, almost simultaneous in-situ data with the SAR acquisition (delay no more than a few hours) throughout the ice season are required for algorithm calibration and validation. However, typically the in-situ measurements are collected in campaigns with a limited spatial and temporal coverage.

In the future the algorithm can be improved by computing the ice motion in a finer scale, taking into account smaller details (narrow straits and river inflows). Also incorporating data from other EO sources for improved thin ice identification will be considered. Application of the algorithms in other ice covered sea areas will also be studied and compared to available ice information.

The new current and upcoming SAR instruments (like RADARSAT-2 and Sentinel-1) have the possibility to acquire dual-polarized data, i.e. both co-polarized (either HH or VV polarization combination) and cross-polarized channels (HV or VH) can be acquired simultaneously. Using cross-polarized SAR data, containing complementary information, in addition to the co-polarized SAR data and can improve the sea ice classification, especially in locating open water, thin ice, and deformed ice areas (Scheuchl, 2004; Geldsetzer and Yackel, 2009). Utilization of dual-polarized SAR data in our algorithms would probably produce improved ice concentration and ice thickness estimates. This would require dual-polarized SAR data of at least one whole ice season over the area of interest. Another advance in the upcoming SAR techniques is that the temporal coverage will considerably be improved as the planned multiple SAR constellations (Sentinel-1, RADARSAT constellation) will be realized. Higher temporal resolution will benefit sea ice motion estimation, and thus improve the ice thickness estimation utilizing the ice motion estimates.

Acknowledgements. The Gulf of Saint Lawrence experiment was funded and the Canadian NWP data were provided by Environment Canada.
The EM ice thickness data was provided by Fisheries and Oceans Canada.

TCD
6, 1871–1914, 2012

References

Andersen, S., Tonboe, R., Kaleschke, L., and Heygster, G.: Intercomparison of passive microwave sea ice concentration retrievals over the high-concentration Arctic sea ice, J. Geophys. Res., 112, C08004, doi:10.1029/2006JC003543, 2007. 1873

Astola, J., Haavisto, P., and Neuvo, Y.: Vector median filters, P. IEEE, 78, 678–689, 1990. 1883

Biazzi, B., Alparone, L., Baronti, S., and Borri, G.: Pyramid-based multi-resolution adaptive filters for additive and multiplicative image noise, IEEE T. Circuits-II, 45, 1092–1097, 1998. 1883

Bitz, C. M., Holland, M. M., Weaver, A. J., and Eby, M.: Simulating the ice-thickness distribution in a coupled climate model, J. Geophys. Res., 106, 2441–2464, 2001. 1874

Briegleb, B. P., Bitz, C. M., Hunke, E. C., Lipscomb, W. H., Holland, M. M., Schramm, J. L., and Moritz, R. E.: Scientific description of the sea ice component in the Community Climate System Model, Version Three. Tech. Rep. NCAR/TN-463+STR, National Center for Atmospheric Research, Boulder, CO, 78 pp., 2004. 1877

Bromwich, D. H., Hines, K. M., and Bai, L.-S.: Development and testing of polar weather research and forecasting model: 2. Arctic Ocean, J. Geophys. Res., 114, D08122, doi:10.1029/2008JD010300, 2009. 1878

Canny, J.: A computational approach to edge detection, IEEE T. Pattern Anal., 8, 679–698, 1986. 1882

Cheng, B., Vihma, T., and Launiainen, J.: Modelling of the superimposed ice formation and sub-surface melting in the Baltic Sea, Geophysica, 39, 31–50, 2003. 1876

Cheng, B., Vihma, T., Pirazzini, R., and Granskog, M.: Modelling of superimposed ice formation during spring snow-melt period in the Baltice Sea, Ann. Glaciol, 44, 139–146, 2006. 1876

Cheng, B., Zhang, Z., Vihma, T., Johansson, M., Bian, L., Li, Z., and Wu, H.: Model experiments on snow and ice thermodynamics in the Arctic Ocean with CHINAREN 2003 data, J. Geophys. Res. 113, C09020, doi:10.1029/2007JC004654, 2008a. 1877, 1878

TCD
6, 1871–1914, 2012

Cheng, B., Vihma, T., Zhang, Z., Li, Z., and Wu, H.: Snow and sea ice thermodynamics in the Arctic: model validation and sensitivity study against SHEBA data, Chinese Journal of Polar Science, 19, 108–122, 2008b. 1877

Dempster, A. P., Laird, N. M., and Rubin, D. B.: Maximum Likelihood from incomplete data via the EM algorithm, J. R. Stat. Soc. B Meth., 39, 1–38, 1977. 1885

DeGroot, M. H.: Probability and Statistics, 3rd edn., Addison-Wesley, Boston, 1991. 1887

Ebert, E. E. and Curry, J. A.: An Intermediate one-dimensional thermodynamic sea ice model for investigating ice-atmosphere interaction, J. Geophys. Res. 98, 10085–10109, 1993.

Fichefet, T. and Maqueda, M. A. M.: Sensitivity of a global sea ice model to the treatment of ice thermodynamics and dynamics, J. Geophys. Res., 102, 609–646, doi:10.1029/97JC00480, 1997. 1874

Flato, G. M. and Brown, R. D.: Variability and climate sensitivity of landfast Arctic sea ice, J. Geophys. Res., 101, 25767–25777, 1996.

Gabison, R.: A thermodynamic model of the formation growth and decay of first-year sea ice, J. Glaciol., 33, 105–109, 1987.

Gao, G., Chen, C., Qi, J., and Beardsley, R. C.: An unstructured-grid, finite-volume sea ice model: development, validation, and application, J. Geophys. Res., 116, C00D04, doi:10.1029/2010JC006688, 2011. 1891

Geldsetzer, T. and Yackel, J. J.: Sea ice type and open water discrimination using dual co-polarized C-band SAR, Can. J. Remote Sens., 35, 73–84, 2009. 1892

Haas, C., Goebell, S., Hendricks, S., Martin, T., Pfaffling, A., and Saldern, C.: Airborne electromagnetic measurements of sea ice thickness: methods and applications, in: Proc. of the workshop Arctic Sea Ice Thickness: Past, Present and Future 2005, Rungstedgaard, Denmark, Nov 8-9, 2005, edited by: Wadhams P. and Amanatidis G. 136–148, ISBN 92–79-02803-EPS, 2006. 1889

Jakobson, E., Vihma, T., Palo, T., Jakobson, L., Keernik, H., and Jaagus, J.: Validation of atmospheric reanalyzes over the Central Arctic Ocean in spring and summer 2007, Geophys. Res. Lett., in press, 2012. 1878

Kaleschke, L., Maaß, N., Haas, C., Hendricks, S., Heygster, G., and Tonboe, R. T.: A sea-ice thickness retrieval model for 1.4 GHz radiometry and application to airborne measurements over low salinity sea-ice, The Cryosphere, 4, 583–592, doi:10.5194/tc-4-583-2010, 2010. 1891

TCD
6, 1871–1914, 2012

Karvonen, J.: Operational SAR-based sea ice drift monitoring over the Baltic Sea, Ocean Sci. Discuss., 9, 359–384, doi:10.5194/osd-9-359-2012, 2012a. 1884
Karvonen, J.: NMF and NTF for sea ice SAR feature extraction and classification, in: Signal and Image Processing for Remote Sensing, 2nd edition, edited by: Chen, C. H., CRC Press, Boca Raton, FL. USA, 117–128, 2012b. 1885
Karvonen, J., Cheng, B., and Similä, M.: Baltic Sea ice thickness charts based on thermodynamic ice model and SAR data, in: Proc. of the International Geoscience and Remote Sensing Symposium 2007 (IGARSS'07), Barcelona, Spain, July 23-27, 2007, 4253–4256, 2007. 1874
Karvonen, J., Cheng, B., and Similä, M.: Ice thickness charts produced by C-band SAR imagery and HIGHTSI thermodynamic ice model, in: Proc. of the Sixth Workshop on Baltic Sea Ice Climate, Lammi, Finland, Aug 25-28, 2008, 71–81, 2008. 1874
Launiainen, J. and Cheng, B.: Modeling of ice thermodynamics in natural water Bodies, Cold Reg. Sci Technol., 27, 153–178, 1998. 1876
Liu, J., Zhang, Z., Inoue, J., and Horton, R. M.: Evaluation of snow/ice albedo parametrization and their impacts on sea ice simulations, Int. J. Climatol., 27, 81–91, 2007. 1877
Luo, Y., Wu, H., Zhang, Y., Sun, C., and Lu, Y.: Application of the HY-1 satellite to sea ice monitoring and forecasting, Acta Oceanol. Sin., 23, 251–266, 2004. 1873
MacQueen, J. B.: Some methods for classification and analysis of multivariate observations, in: Proceedings of 5th Berkeley Symposium on Mathematical Statistics and Probability, Berkeley, CA, USA, 12 June – 18 July 1965, 27 December 1965 – 7 January 1966, University of California Press, 281–297, 1967. 1881
Mäkynen, M. and Hallikainen, M.: Investigation of C- and X-band backscattering of Baltic Sea ice, Int. J. Remote Sens., 25, 2061–2086, 2004. 1873, 1886
Mäkynen, M., Manninen, T., Similä, M., Karvonen, J., and Hallikainen, M.: Incidence angle dependence of the statistical properties of the C-Band HH-polarization backscattering signatures of the Baltic Sea ice, IEEE T. Geosci. Remote, 40, 2593–2605, 2002. 1881
Mäkynen, M., Similä, M., and Cheng, B.: On level ice thickness retrieval in the Kara Sea using MODIS and ENVISAT ASAR data, in: Proc. of ESA Living Planet Symposium 2010, Bergen, Norway, June 28 - July 2, 2010, CD ESA SP-686, 2010. 1891
Maykut, G. A. and Untersteiner, N.: Some results from a time-dependent thermodynamic model of sea ice, J. Geophys. Res., 76, 1550–1575, 1971.

TCD
6, 1871–1914, 2012

Ojala, T., Pietikäinen, M., and Harwood, D.: A comparative study of texture measures with classification based on feature distributions, Pattern Recogn., 29, 51–59, 1996. 1884

Pfaffling, A., Haas, C., and Reid, J. E.: Key characteristics of helicopter electromagnetic sea ice thickness mapping resolution, accuracy and footprint, in: Proc. of the workshop Arctic Sea Ice Thickness: Past, Present and Future 2005, Rungstedgaard, Denmark, Nov 8-9, 2005, edited by: Wadhams P. and Amanatidis G., 46–56, ISBN 92-79-02803-EPS, 2006. 1889

Pringle, D. J., Eicken, H., Trodahl, H. J., and Backstrom, L. G. E.: Thermal conductivity of landfast Antarctic and Arctic sea ice, J. Geophys. Res., 112, C04017, doi:10.1029/2006JC003641, 2007. 1877

Prinsenberg, S. J., Holladay, S., and Lee, J.: Measuring ice thickness with EISFlow, a fixed-mounted helicopter electromagnetic-laser system, Int. Offshore Polar E., 1, 737–740, 2002. 1889

Sandven, S. and Johannesen, O. M.: Sea ice monitoring by remote sensing, in: Manual of Remote Sensing: Remote Sensing of the Marine Environment, edited by: Gower, J. F. R., 3rd edn., Bethesda, American Society for Photogrammetry & Remote Sensing, vol. 6, 241–283, 2006. 1873

Scheuchl, B., Flett, D., Caves, R., and Cumming, I.: Potential of RADARSAT-2 data for operational sea ice monitoring, Can. J. Remote Sens., 30, 448–461, 2004. 1892

Semmler, T., Cheng, B., Yang, Y., and Rontu, L.: Snow and ice on Bear Lake (Alaska) – sensitivity experiments with two lake ice models, Tellus A 2012, v. 64, doi:10.3402/tellusa.v64i0.17339, 2012. 1877

Shokr, M.: Compilation of a radar backscatter database of sea ice types and open water using operational analysis of ice regimes, Can. J. Remote Sens., 35, 369–384, 2009. 1873, 1886

Tietäväinen, H. and Vihma, T. Atmospheric moisture budget over Antarctica and Southern Ocean on the basis of ERA-40 reanalysis, Int. J. Climatol., 28, 1977–1995, doi:10.1002/joc.1684, 2008. 1878

Thomas, M., Geiger, C., and Kambhamettu, C.: Discontinuous Non-Rigid Motion Analysis of Sea Ice using C-Band Synthetic Aperture Radar Satellite Imagery, IEEE Workshop on Articulated and Nonrigid Motion (ANM, In conjunction with CVPR'04), available at: http://vims.cis.udel.edu/publications/anm-thomas.pdf, accessed May 23, 2012, 2004. 1882

Vihma, T., Uotila, J., Cheng, B., and Launiainen, J.: Surface heat budget over the Weddell Sea: buoy results and comparisons with large-scale models, J. Geophys. Res., 107, C2, doi:10.1029/2000JC000372, 2002. 1876

Wessel, P. and Smith, W. H. F.: A global self-consistent, hierarchical, high-resolution shoreline database, J. Geophys. Research, 101, 8741–8743, 1996. 1881

Yang, Y., Leppäranta, M., Cheng, B., and Li, Z.: Numerical modelling of snow and ice thickness in Lake Vanajavesi, Finland, Tellus A, 64, 17202, doi:10.3402/tellusa.v64i0.17202, 2012. 1877

Yu, Y. and Rothrock, D. A.: Thin ice thickness from satellite thermal imagery, J. Geophys. Res., 101, 25753–25766, 1996. 1891

TCD

6, 1871–1914, 2012

Table 1. Conversion from the egg-code stage of development into ice thickness used here. The multi-year ice types have been excluded.

Egg code	Stage of dev.	Thickness (cm)
1	New ice	5
2	Nilas ice	10
3	Young ice	15
4	Gray ice	15
5	Gray-white ice	30
6	1st-year ice	50
7	Thin 1st-year ice	70
8	1st-year thin – 1st stage	70
9	1st-year thin – 2nd stage	70
1.	Medium 1st-year ice	120
4.	Thick 1st-year ice	140
	Fast ice	120

TCD
6, 1871–1914, 2012

Table 2. Conversion from the CIS egg-code total concentration (C_t, given in tenths) into ice concentration shown in this paper. The egg-code labels OW and IF are converted to 0 % and FAST (fast ice) to 100 %.

Egg code	1	1+	2	2+	3	3+	4	4+	5	5+	6	6+	7	7+	8	8+	9	9+	10
Concentr (%).	10	15	20	25	30	35	40	45	50	55	60	65	70	75	80	85	90	95	100

TCD
6, 1871–1914, 2012

Table 3. Kolmogorov-Smirnov statistics compared to the EM ice thickness.

Season	SAR algor.	HIGHTSI	CIS IC
2002–2003	0.194	0.646	0.347
2008–2009	0.180	0.624	0.675

TCD
6, 1871–1914, 2012

Table 4. Mean ice thickness (in cm) according to different sources along the EM flight lines for the two seasons.

Source	2002–2003	2008–2009
SAR algor.	52.0	59.1
CIS IC	15.2	18.8
HIGHTSI	40.4	23.1
EM	49.3	47.7

TCD
6, 1871–1914, 2012

Fig. 1. The Gulf of St Lawrence and surroundings plotted in Lambert Conformal Conic (LCC) projection. The ice analysis domain is the red-dotted sea area; each dot corresponds to one grid cell of the ice model. The original model domain is computed in latitude-longitude and then converted to LCC. The corner latitudes and longitudes of the original grid are shown. The ice model simulations are made at each grid cell for the two winter seasons.

TCD
6, 1871–1914, 2012

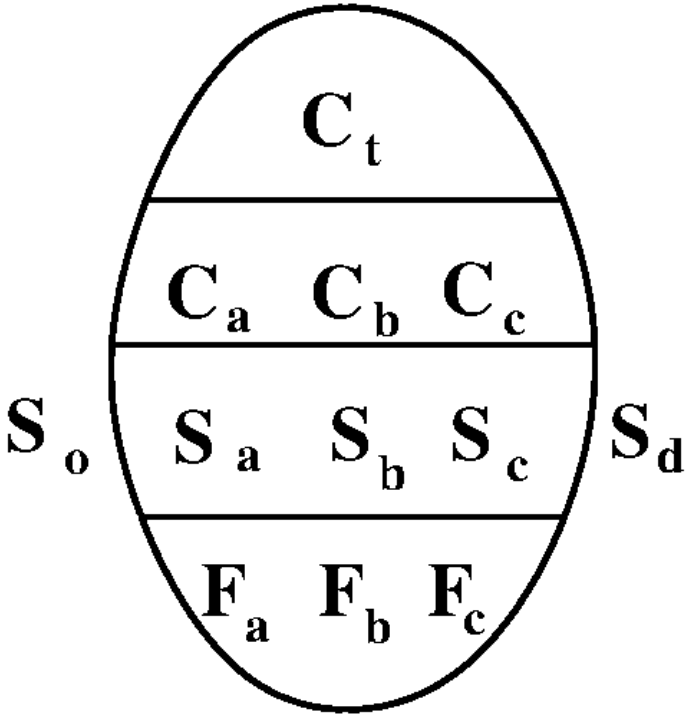

Fig. 2. The WMO egg code given for each polygon (area). C_t is the total concentration, C_a, C_b, C_c are the partial concentrations, S_a, S_b, S_c are the partial stages of development corresponding to the partial concentrations, and F_a, F_b, F_c are the partial predominant forms of ice. S_o and S_d are the stages of development of the possible remaining ice types within the the area. All three partial values are not necessarily assigned for each polygon, if there are less ice types present according to the ice analyst interpretation.

TCD
6, 1871–1914, 2012

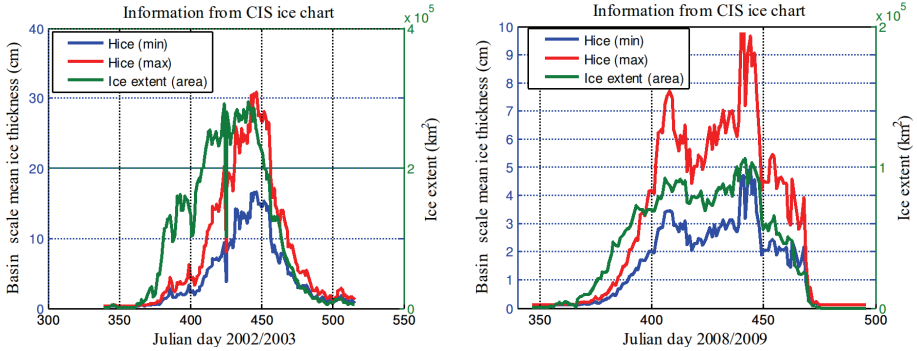

Fig. 3. Time series of ice extent and maximum and minimum ice thickness retrieved from operational CIS ice charts for winters **(a)** 2002/2003 and **(b)** 2008/2009.

TCD
6, 1871–1914, 2012

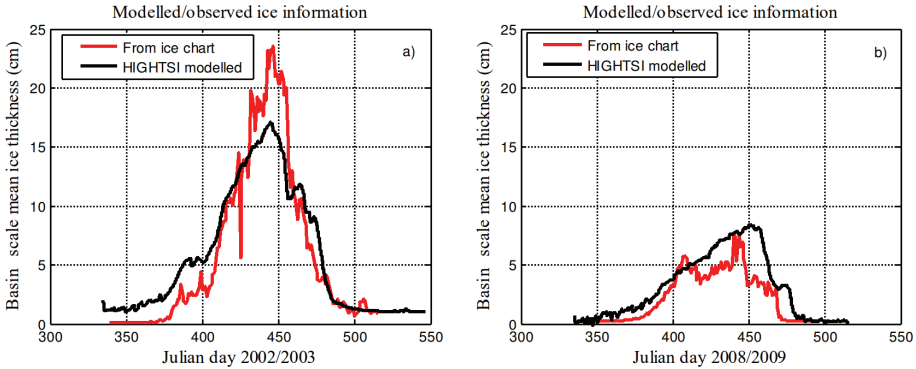

Fig. 4. Observed and modeled basin scale average ice thickness for winter season 2002/2003 **(a)** and 2008/2009 **(b)**.

TCD
6, 1871–1914, 2012

Fig. 5. An example of a SAR mosaic (based on RADARSAT-2 data,© MDA), on 5 March 2009, the boundaries between SAR frames have been smoothed in the mosaic.

TCD
6, 1871–1914, 2012

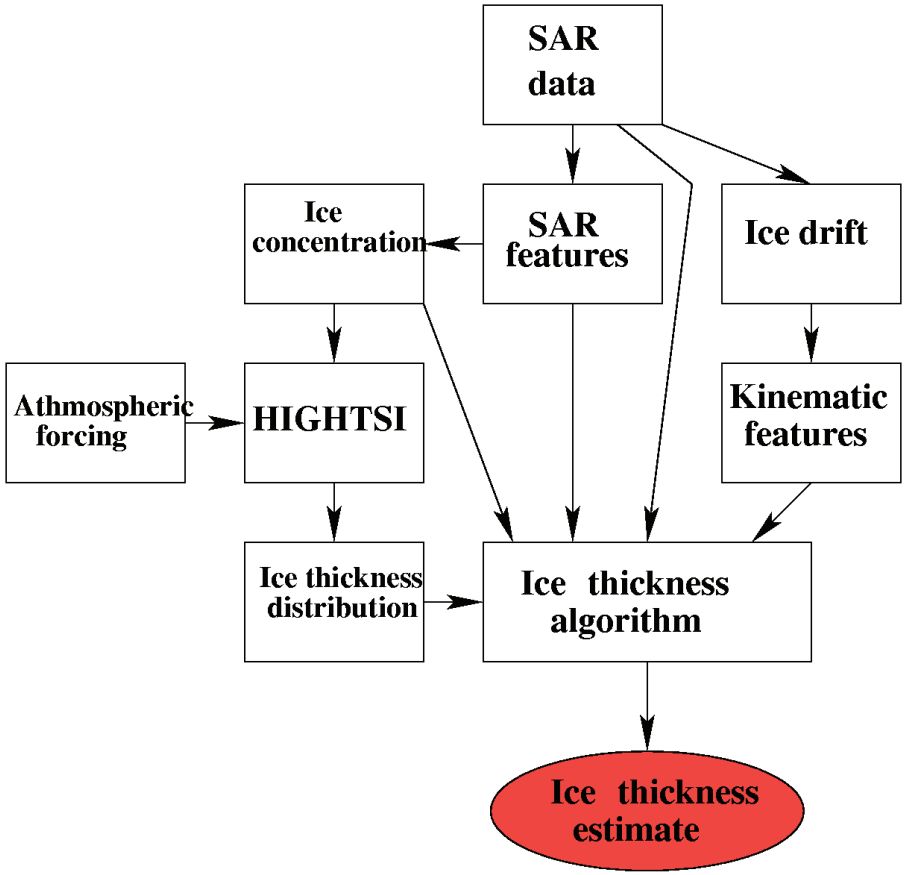

Fig. 6. A general block diagram of the ice thickness algorithm.

TCD
6, 1871–1914, 2012

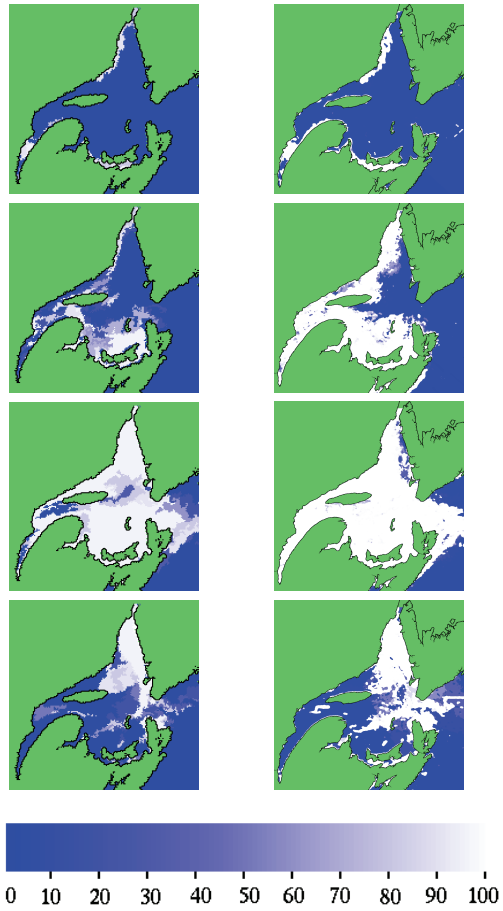

Fig. 7. Ice concentration for the 5 Januar, 5 Februar, 5 March, and 5 April 2003 (from top to bottom), from the CIS ice charts (left column) and based on our SAR algorithm (right column).

TCD
6, 1871–1914, 2012

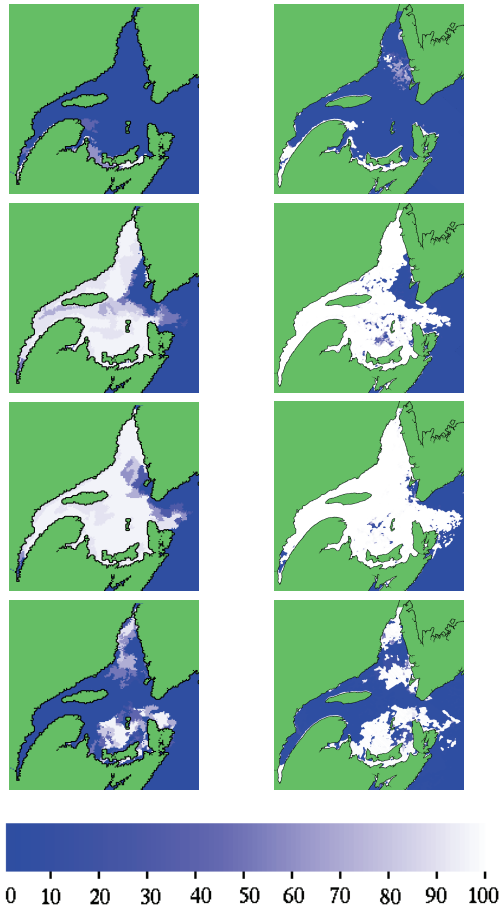

Fig. 8. Ice concentration for the 5 Januar, 5 Februar, 5 March, and 5 April 2009 (from top to bottom), from the CIS ice charts (left column) and based on our SAR algorithm (right column).

TCD
6, 1871–1914, 2012

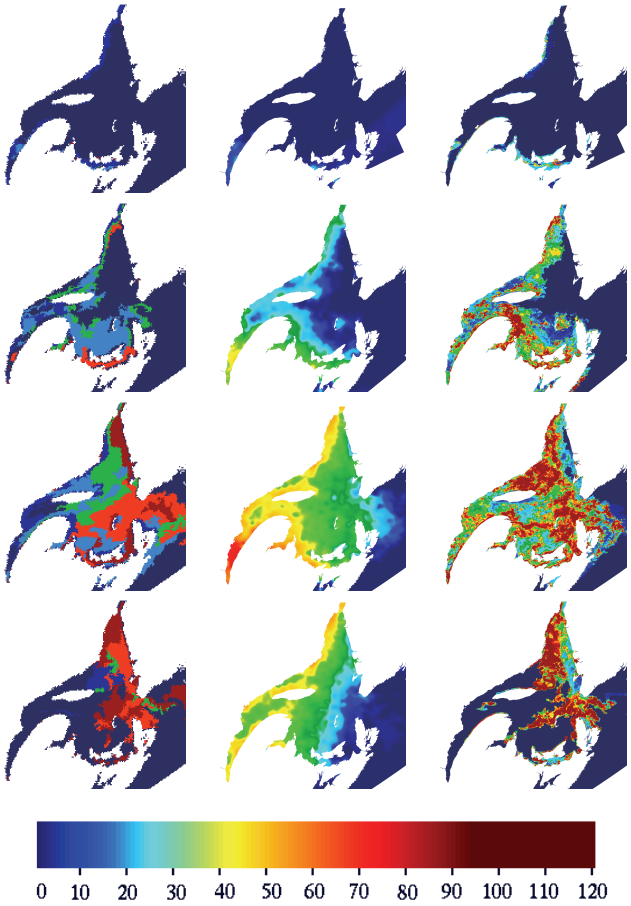

Fig. 9. Ice thickness for the 5 Januar, 5 Februar, 5 March, and 5 April 2003 (from top to bottom), from the CIS ice charts (left column), from HIGHTSI model (middle column), and based on our SAR algorithm (right column).

TCD
6, 1871–1914, 2012

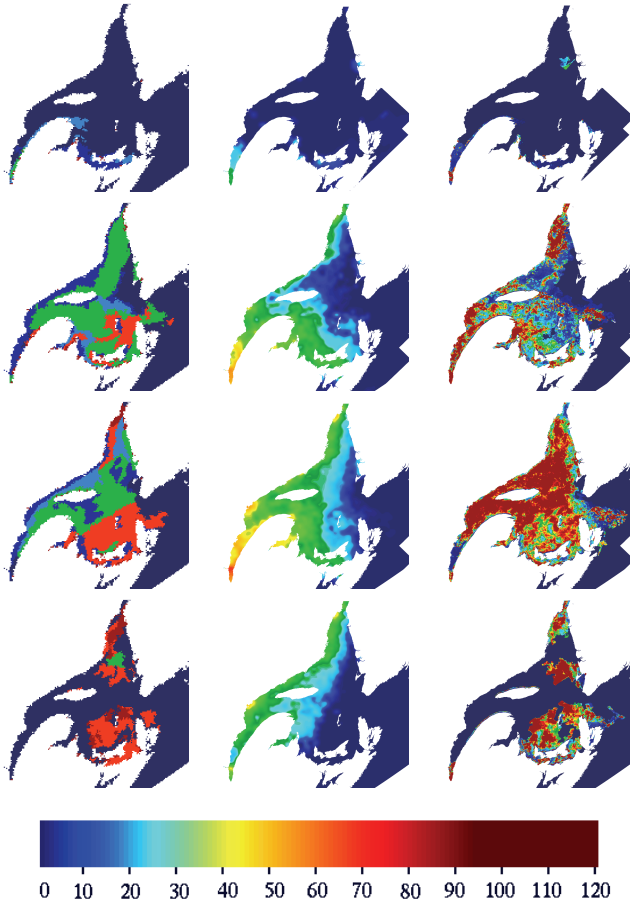

Fig. 10. Ice thickness for the 5 Januar, 5 Februar, 5 March, and 5 April 2009 (from top to bottom), from HIGHTSI model (middle column), from the CIS ice charts (left column) and based on our SAR algorithm (right column).

TCD
6, 1871–1914, 2012

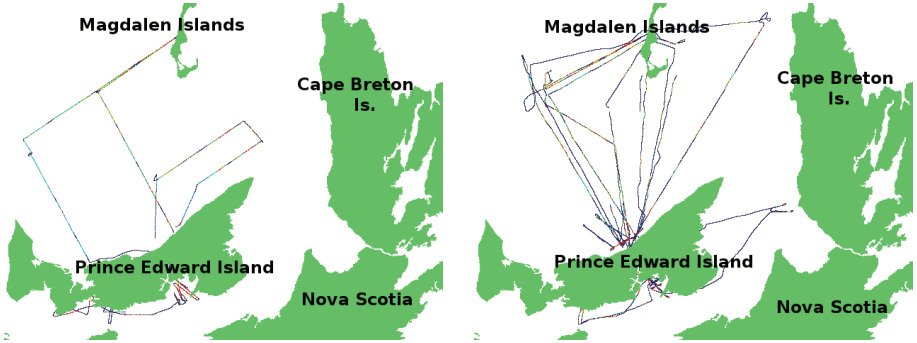

Fig. 11. The EM flights in 2003 (left) and 2009 (right).

TCD
6, 1871–1914, 2012

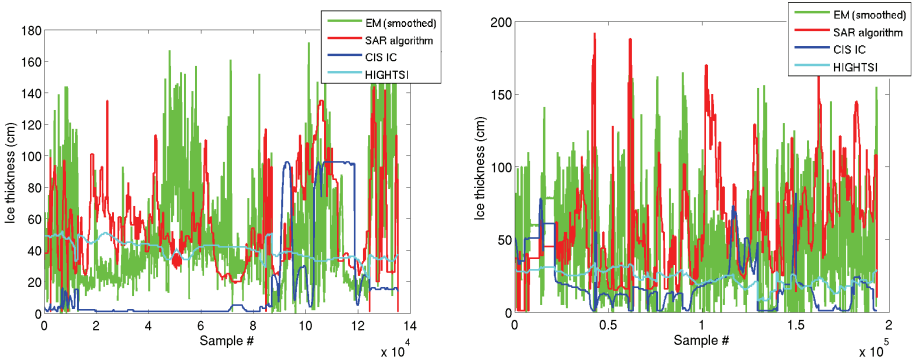

Fig. 12. The ice SAR algorithm thickness compared to HIGHTSI ice thickness, mean ice thickness derived from digitized CIS ice charts, and EM ice thickness measurements for the two test seasons.

TCD
6, 1871–1914, 2012

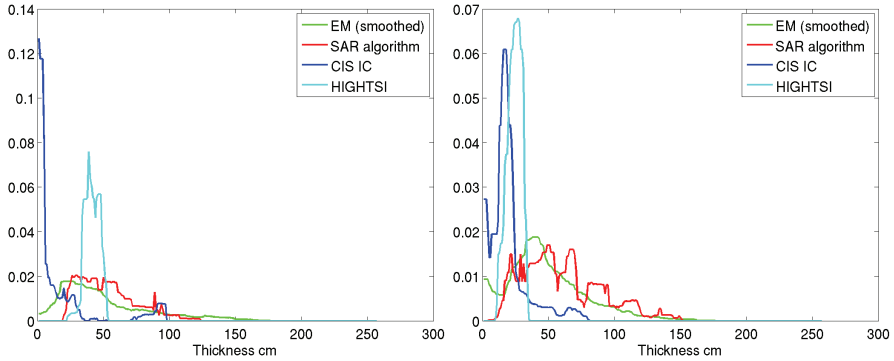

Fig. 13. The ice thickness distributions from different sources along the EM measurement lines for both the test seasons, 2002–2003 on the left and 2008–2009 on the right.

TCD
6, 1871–1914, 2012